Geometrical analysis of the LiCN vibrational dynamics: A stability geometrical indicator

A. Vergel,[*] R. M. Benito,[†] and J. C. Losada[‡]

Grupo de Sistemas Complejos, Universidad Politécnica de Madrid, 28040 Madrid, Spain and Departamento de Física y Mecánica, Escuela Técnica Superior de Ingenieros Agrónomos, Universidad Politécnica de Madrid, 28040 Madrid, Spain

F. Borondo[§]

Departamento de Química, Universidad Autónoma de Madrid, Cantoblanco, 28049–Madrid, Spain and Instituto de Ciencias Matemáticas (ICMAT), Cantoblanco, 28049–Madrid, Spain

(Received 26 September 2013; revised manuscript received 18 December 2013; published 3 February 2014)

The vibrational dynamics of the LiNC/LiCN molecular system is examined making use of the Riemannian geometry. Stability and chaoticity are analyzed, in this context, by means of the Jacobi-Levi-Civita equations, derived from the Jacobi metric, and its solutions. A dynamical indicator, called *stability geometrical indicator*, is introduced in order to ascertain the dynamical characteristics of stability and chaos in the molecule under study.

DOI: 10.1103/PhysRevE.89.022901 PACS number(s): 05.45.Mt

I. INTRODUCTION

The vibrational dynamics of highly excited molecular systems, which usually has a strong chaotic component in floppy molecules [1], is a topic of much interest due to its relevance in many interesting chemical processes, such as unimolecular and isomerization reactions, photodissociation, or intramolecular energy relaxation [2]. Laser technology and other new experimental techniques have made the experimental observation of these processes possible [3], even in real time [4].

Although, extensive work has been published on the formal aspects of the general theory of chaos in Hamiltonian systems, simple chaos indicators are desirable for practical applications. Among them, maximum Lyapunov exponents (LE) [5], fast Lyapunov indicator [6,7], frequency map analysis [8], and the small alignment index (SALI) [9] are worth mentioning. Also, some applications to molecular systems have been presented along this line in the literature [10,11].

Another interesting method consists in recasting the corresponding dynamics in a Riemann geometry, so that the instability of the geodesic flow is solely determined by the curvature of the suitable manifolds [12,13]. Different metrics have been defined for this purpose in literature, such as those due to Eisenhart [14], Finsler [15], Horwitz [16,17], or Jacobi [18–23]. In our case, we choose the Jacobi metric derived from the Maupertuis' principle, where geodesics [24], i.e., the natural motions, in the mechanical manifold are identified with trajectories of the system, and their stability can be analyzed through the study of the curvature of this Riemannian manifold, via the Jacobi-Levi-Civita equations (JLC) [24]. This conceptual framework allows one to understand Hertz's curvature principle in a natural way, as well as the importance of directions perpendicular to the trajectories in order to study their stability. Notice that this geometrical interpretation is not just a mere rewriting of the system dynamics, but more importantly, it points to what appears to be a fundamental characterization of Hamiltonian chaos. The reason for this is simple. A negative curvature produces a spreading of the trajectories close to a fiducial one, something that is related to the origin of chaos in the Lyapunov sense. Moreover, when the curvature is positive the chaotic behavior springs out as the result of a mechanism originated by the fluctuation of the scalar curvature along the fiducial geodesic [20]. The evolution for the deviation vector, measuring the geodesic spreading, is the main criterion for the onset of chaos. It can be described as a harmonic oscillator equation, where the frequency is replaced by scalar curvature, so that its fluctuation along the fiducial trajectory is the origin of the phenomenon called parametric resonance, as in the Mathieu's equation [21,25]. This approach has been successfully applied to the LE calculation for Hamiltonian systems with many degrees of freedom [22] by doing a previous coarse-grained simplification of the corresponding JLC equations.

The aim of this paper is the study the instability properties of the nonlinear Hamiltonian dynamics of the LiNC and LiCN molecular isomerization system using the geometric methods described above. The phase-space structure for the vibrational dynamics for the LiCN molecule has been extensively studied in the past [26,27] using a realistic model potential [28]. For this purpose, we introduce a stability geometrical indicator (SGI) to quantitatively gauge the stability of different vibration trajectories, chosen as representative examples of the LiNC dynamics.

The organization of the paper is as follows. In Sec. II the geometrical approach for a Hamiltonian system is described, relating chaos with the JLC equations. In Sec. III the model used for LiNC and LiCN is discussed and the corresponding metrics and specific JLC expressions are given. In Sec. IV we present our results for representative trajectories of LiNC and LiCN for both the dynamical and geometrical descriptions, as well as the SGI criterion. Finally, the main conclusions are summarized in Sec. V.

[*]alberto.vergel.otero@alumnos.upm.es
[†]rosamaria.benito@upm.es
[‡]juancarlos.losada@upm.es
[§]f.borondo@uam.es

II. GEOMETRICAL APPROACH FOR A DYNAMICAL SYSTEM

A. Dynamics recast into geodesics: The Riemannian manifold

We start by considering a generic Lagrangian (hereafter we use Einstein's summation convention),

$$\mathcal{L}(\dot{\mathbf{q}},\mathbf{q}) = \tfrac{1}{2}\, a_{ij}(\mathbf{q})\, \dot{q}^i \dot{q}^j - V(\mathbf{q}), \tag{1}$$

where the mass tensor fulfills $a_{ij}a^{ik} = \delta^k_j$, and the conjugate momenta are defined as $P_i = d\mathcal{L}/d\dot{q}^i$.

As it is well known, Maupertuis' principle establishes that the natural motions for this system are those whose trajectories make extremal the action integral $\int_{\gamma(t)} P_i dq^i$. In a case, like the one considered here, where the energy, $E = W(\mathbf{P}) + V(\mathbf{q})$, is conserved, this is equivalent to

$$\delta \int_{\gamma(t)} \sqrt{2[E - V(\mathbf{q})]\, a_{ij}(\mathbf{q})\, \dot{q}^i \dot{q}^j}\; dt = \delta \int_{\gamma(s)} ds = 0, \tag{2}$$

so that the trajectories correspond to geodesics in a Riemannian differentiable manifold endowed with the metric defined by

$$ds^2 = g_{ij}(\mathbf{q})\, dq^i dq^j = 2[E - V(\mathbf{q})]\, a_{ij}(\mathbf{q})\, dq^i dq^j, \tag{3}$$

where g_{ij} corresponds to what it is known as the Jacobi metric. The system configuration space is the previous Riemannian manifold where $\{\mathbf{q}\}$ represents the local coordinates, and is often referred to as the mechanical manifold $[M, g_{ij}(\mathbf{q})]$. It can be shown that the trajectory followed by a particle affected by the potential $V(\mathbf{q})$ in the Euclidean space is equivalent to the motion of a free particle in the mechanical manifold. In this way, there is a correspondence between the dynamics in an Euclidean space (zero curvature) and the kinematics in a non-Euclidean space with curvature. Geodesics are autoparallel curves described by

$$\begin{aligned}\nabla_{\dot\gamma}\dot\gamma &= \nabla_{\frac{d\gamma}{ds}}\left(\frac{d\gamma}{ds}\right)\\ &= \frac{D}{ds}\left(\frac{d\gamma}{ds}\right) = \frac{d^2q^i}{ds^2} + \Gamma^i_{jk}\frac{dq^j}{ds}\frac{dq^k}{ds} = 0,\end{aligned} \tag{4}$$

where D/ds is the covariant derivative along the curve $\gamma(s)$, s is the arc-length parameter, and Γ^i_{jk} are the so-called Christoffel symbols associated to the metric g_{ij}, which are given by

$$\begin{aligned}\Gamma^i_{jk} &= \frac{1}{2}\, g^{im}\,(\partial_j g_{km} + \partial_k g_{mj} - \partial_m g_{jk})\\ &= -\frac{1}{2W}\left[\delta^i_k \partial_j V + \delta^i_j \partial_k V - \partial_l V\, a^{li} a_{jk}\right]\\ &\quad + \frac{1}{2}\, a^{il}[-\partial_l\, a_{jk} + \partial_k\, a_{lj} + \partial_j\, a_{lk}],\end{aligned} \tag{5}$$

where W is the kinetic energy. Finally, by changing from s to t in Eq. (4), we obtain the differential equation for the geodesics as

$$\frac{d^2q^i}{dt^2} + \frac{1}{W}\left(\frac{\partial V}{\partial q^l}\frac{dq^l}{dt}\right)\frac{dq^i}{dt} + \Gamma^i_{jk}\frac{dq^j}{dt}\frac{dq^k}{dt} = 0. \tag{6}$$

We conclude this subsection by presenting in Table I the equivalence between some relevant magnitudes in the dynamical and geometrical views of the classical mechanics.

TABLE I. Equivalence between some relevant magnitudes in the dynamical and geometrical views of the classical mechanics.

Dynamics	Geometry
Time, t	Arc-length, s
Potential, V	Metric, g_{ij}
Force, ∂V	Christoffel symbols, Γ^i_{jk}
Trajectories	Geodesics
Conserved quantities	Symmetries
Instability	Curvature

B. Curvature and chaos: The JLC equations

The sectional curvature $K(p,\sigma)$ at point $p \in M$ and tangent plane $\sigma \subset T_pM$ on the Riemannian manifold M at this point determines the spreading rate for the geodesics starting at point p and tangent to M. (Notice that K corresponds to the Gaussian curvature in the bidimensional case.)

The evolution of this geodesic deviation, $\mathbf{J}(s)$, from the fiducial trajectory $\gamma(s)$ is given by the so-called JLC equations,

$$\frac{D^2\mathbf{J}}{ds^2} + R[\dot\gamma(s),\mathbf{J}(s)]\,\dot\gamma(s) = 0, \tag{7}$$

with $\gamma : s \in [0,a] \to M$ geodesic in M, $\dot\gamma(s) = d\mathbf{q}/ds$, and $R(\mathbf{X},\mathbf{Y}) : T_pM \longrightarrow T_pM$, given by $R(X,Y)Z = \nabla_X\nabla_Y Z - \nabla_Y\nabla_X Z - \nabla_{[X,Y]}Z$, with $X,Y,Z \in T_pM$, is the so called Riemann-Christoffel curvature tensor.

In actual applications, local coordinates $\{\mathbf{e}_i\}$ are used, and Eq. (7) takes the form

$$\frac{D^2J^i}{ds^2} = -S^i_{jkl}\dot\gamma^j\dot\gamma^l J^k = -S^i_k J^k, \tag{8}$$

with S^i_k being the stability tensor. In this reference frame,

$$R(\mathbf{e}_i,\mathbf{e}_j)\mathbf{e}_k = R^l_{ijk}\mathbf{e}_l, \tag{9}$$

with

$$R^l_{ijk} = \Gamma^s_{ik}\Gamma^l_{js} - \Gamma^s_{jk}\Gamma^l_{is} + \frac{\partial\Gamma^l_{ik}}{\partial x_j} - \frac{\partial\Gamma^l_{jk}}{\partial x_i}. \tag{10}$$

Furthermore, Eq. (7) can be expressed in a more convenient moving frame, formed by an orthonormal vectors set $\{\mathbf{e}_{(1)},\mathbf{e}_{(2)}\}$ transported in a parallel way along $\gamma(s)$

$$\mathbf{e}_{(i)} = \mathbf{e}^j_{(i)}\mathbf{e}_j, \quad i = 1,2, \tag{11}$$

where $\nabla\mathbf{e}_{(i)}/ds \equiv D\mathbf{e}_{(i)}/ds = 0$. Again, in local coordinates these expressions simplify, becoming equivalent to $[(d\mathbf{e}^\alpha_{(i)}/dt) + \mathbf{e}^\mu_{(i)}\Gamma^\alpha_{\mu\beta}(dq^\beta/dt)]\mathbf{e}_\alpha = 0$. As a result, the components $\mathbf{e}^\alpha_{(i)}$ for the parallel transported vectors $\mathbf{e}_{(i)}$ can be calculated using a Taylor expansion: $\mathbf{e}^\alpha_{(i)}|_t = \mathbf{e}^\alpha_{(i)}|_{t_0} - \mathbf{e}^\mu_{(i)}\Gamma^\alpha_{\mu\beta}(dq^\beta/dt)|_{t_0}(t - t_0) + \mathcal{O}(t - t_0)^2$. The previous process is equivalent, only in dimension two, to imposing the orthonormality condition

$$g_{ij}(\mathbf{q})\, \mathbf{e}^i_{(a)}\mathbf{e}^j_{(b)} = \delta_{ab}. \tag{12}$$

Setting the tangent vector to the fiducial trajectory, $\mathbf{e}_{(1)}(s) = \dot\gamma(s)$, as the initial vector, at any point on this curve one obtains

the new moving frame as

$$\begin{aligned}\mathbf{e}_{(1)}(s) &= \dot{\gamma}^1(s)\,\mathbf{e}_1(s) + \dot{\gamma}^2(s)\,\mathbf{e}_2(s)\\ \mathbf{e}_{(2)}(s) &= \sqrt{a_{22}/a_{11}}\,\dot{\gamma}^2\,\mathbf{e}_1(s) - \sqrt{a_{11}/a_{22}}\,\dot{\gamma}^1\,\mathbf{e}_2(s).\end{aligned} \tag{13}$$

Notice that these conditions only depend on the tangent vector and the point, which is not so in higher dimensions. In the new frame, $\{\mathbf{e}_{(1)},\mathbf{e}_{(2)}\}$, the vector field $\mathbf{J}(s)$ is expressed as $\mathbf{J}(s) = J^i(s)\mathbf{e}_{(i)}(s), i = 1,2$, and then Eq. (7) becomes

$$\begin{pmatrix}\frac{d^2J^1}{ds^2}\\ \frac{d^2J^2}{ds^2}\end{pmatrix} + \begin{pmatrix}\langle R(\mathbf{v},\mathbf{e}_{(1)})\mathbf{v},\mathbf{e}_{(1)}\rangle & \langle R(\mathbf{v},\mathbf{e}_{(2)})\mathbf{v},\mathbf{e}_{(1)}\rangle\\ \langle R(\mathbf{v},\mathbf{e}_{(1)})\mathbf{v},\mathbf{e}_{(2)}\rangle & \langle R(\mathbf{v},\mathbf{e}_{(2)})\mathbf{v},\mathbf{e}_{(2)}\rangle\end{pmatrix}\begin{pmatrix}J^1\\ J^2\end{pmatrix} = 0, \tag{14}$$

where $\langle,\rangle$ is the inner product, and $\langle\mathbf{e}_i,\mathbf{e}_j\rangle = g_{ij}$ are the metric coefficients (first fundamental form). Now, if $\mathbf{v} = \mathbf{e}_{(1)} = \dot{\gamma}$ and considering the curvature tensor symmetries, i.e., $\langle R(\mathbf{e}_i,\mathbf{e}_j)\mathbf{e}_k,\mathbf{e}_l\rangle = R_{ijkl} = R_{klij} = -R_{jikl} = -R_{ijlk}$, Eq. (14) can be reduced to

$$\begin{pmatrix}\frac{d^2J^1}{ds^2}\\ \frac{d^2J^2}{ds^2}\end{pmatrix} + \begin{pmatrix}0 & 0\\ 0 & \langle R(\mathbf{e}_{(1)},\mathbf{e}_{(2)})\mathbf{e}_{(1)},\mathbf{e}_{(2)}\rangle\end{pmatrix}\begin{pmatrix}J^1\\ J^2\end{pmatrix} = 0. \tag{15}$$

Taking into account that

$$|\mathbf{e}_{(1)}\wedge\mathbf{e}_{(2)}| = \sqrt{|\mathbf{e}_{(1)}|^2|\mathbf{e}_{(2)}|^2 - \langle\mathbf{e}_{(1)},\mathbf{e}_{(2)}\rangle^2} = 1, \tag{16}$$

where $\wedge$ denotes the outer product, we can write that

$$\begin{aligned}\langle R(\mathbf{e}_{(1)},\mathbf{e}_{(2)})\mathbf{e}_{(1)},\mathbf{e}_{(2)}\rangle &= \frac{\langle R(\mathbf{e}_{(1)},\mathbf{e}_{(2)})\mathbf{e}_{(1)},\mathbf{e}_{(2)}\rangle}{|\mathbf{e}_{(1)}\wedge\mathbf{e}_{(2)}|^2}\\ &= K(\mathbf{e}_{(1)},\mathbf{e}_{(2)}) \equiv K(\sigma),\end{aligned} \tag{17}$$

where $K(\sigma)$ is the sectional curvature for the plane generated by $\mathbf{e}_{(1)}$ and $\mathbf{e}_{(2)}$ at $\gamma(s)$, which can also be expressed in local coordinates as

$$\begin{aligned}K(\sigma) = K(\mathbf{e}_{(1)},\mathbf{e}_{(2)}) &= \frac{R_{ljhk}e^l_{(1)}e^h_{(1)}e^j_{(2)}e^k_{(2)}}{(g_{lh}g_{jk} - g_{lk}g_{jh})e^l_{(1)}e^h_{(1)}e^j_{(2)}e^k_{(2)}}\\ &= \frac{1}{|\,g_{ij}\,|}R_{1212} = \frac{\hat{R}}{2},\end{aligned} \tag{18}$$

where $\hat{R}$ is the scalar curvature. We can write Eq. (15) as

$$\begin{aligned}\frac{d^2J^1}{ds^2} &= 0\\ \frac{d^2J^2}{ds^2} &= -\frac{R_{1212}}{|g_{ij}|}J^2 = -\frac{\hat{R}(s)}{2}J^2.\end{aligned} \tag{19}$$

The evolution of J^1 is at most linear and the stability is determined by the scalar J^2 (from now on referred to as J) along the fiducial curve. Notice that the stability tensor is pointwise and does not depend on the evolution of the basis vectors, contrary to what happens in more dimensions.

Fixing a constant length s for the trajectory, we define, in the spirit of the exponential separation implied by a positive Lyapunov exponent [5–7], the dynamical magnitude SGI(s) as a *stability geometrical indicator* of chaos, as

$$\mathrm{SGI}(s,\mathbf{x_0}) = \max_{0\leqslant s'\leqslant s}[J(s',\mathbf{x_0})], \tag{20}$$

with the $J(s',\mathbf{x}_0)$ component J^2 for s', and initial conditions $\mathbf{x}_0$.

We will use this indicator to compare the mutual relative stabilities for different trajectories.

III. SYSTEM AND CALCULATIONS

A. The model

The system that we have chosen to illustrate our method is the LiNC and LiCN isomerizing system.

This molecule presents two stable isomers at the linear configurations: Li–N–C and Li–C–N, which are separated by a relatively modest energy barrier of only 0.0157376 a.u. The motion in the bending coordinate is very floppy, i.e., it is a large-amplitude motion, which samples ample nonharmonic regions of the potential energy surface, even rotating around the C–N fragment. In this way, chaos sets in at low values of the excitation energy. Moreover, the vibrational frequency of the C–N motion is very high, and then this mode is not strongly coupled with the other vibrations in the molecule. As a result, the vibrations of this molecular system can be adequately studied by a two degrees of freedom model with the NC distance frozen at its equilibrium value ($r_e = 2.186$ a.u.). The corresponding rotationless classical Hamiltonian is given by

$$H = \frac{P_R^2}{2\mu_1} + \frac{1}{2}\left(\frac{1}{\mu_1 R^2} + \frac{1}{\mu_2 r_e^2}\right)P_\theta^2 + V(R,\theta), \tag{21}$$

where R is the distance from the NC center of mass to the Li atom, r_e is the NC distance, and θ is the angle defined by the corresponding vectors. Also, P_R and P_θ are the associated conjugate momenta, and $\mu_1 = m_{\mathrm{Li}}^{-1} + m_{\mathrm{CN}}^{-1}$ and $\mu_2 = m_{\mathrm{C}}^{-1} + m_{\mathrm{N}}^{-1}$ represent the Li–CN and C–N reduced masses, respectively. The potential energy surface, $V(R,\theta)$, which consists of an analytical expansion in terms of Legendre polynomials,

$$V(R,\theta) = \sum_{\lambda=0}^{9} v_\lambda(R)P_\lambda(\cos\theta), \tag{22}$$

with coefficients fitted to *ab initio* quantum mechanical calculations, has been taken from the literature [28], and it is shown in Fig. 1 in the form of a contours plot. As can be seen, it presents two minima at $\theta = 0$ and 180°, corresponding to the two linear isomers LiCN and LiNC, respectively. The minimum energy path, $R_e(\theta)$, connecting these two isomers is given by the expression

$$R_e(\theta) = \sum_{\lambda=0}^{9} b_\lambda\cos(\lambda\theta), \tag{23}$$

where the numerical values for the coefficients are given in Table II, and it has also been included in Fig. 1, as a dashed line. The corresponding energy profile, $V_e = V[R_e(\theta),\theta]$, is given in the top panel of the plot.

B. Classical trajectories calculation

To help in the discussion we will use for comparison some trajectory calculations. They are numerically propagated using a fourth-order Runge-Kutta method. The motion in the angular coordinate, θ, is very floppy, and then chaos sets in at very modest excitation energy. These dynamics are best monitored

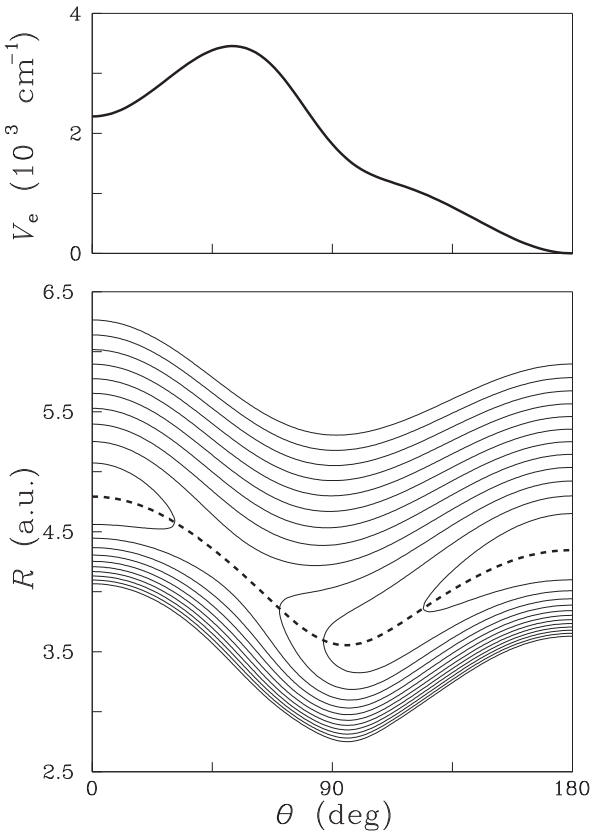

FIG. 1. (Bottom) Potential energy surface for the LiNC and LiCN isomerizing system. Contour lines have been plotted every 1000 cm^{-1}. The minimum energy path connecting the two isomers is shown as a dashed line. (Top) Energy profile along the minimum energy path.

by PSOS, which are computed taking the minimum energy path, $R_e(\theta)$, as the sectioning plane [29]. This PSOS is made an area preserving map defining a new set of canonical variables:

$$\begin{aligned} &\rho = R - R_e(\theta), \quad P_\rho = P_R\ , \\ &\psi = \theta, \quad P_\psi = P_\theta + \left(\frac{dR_e}{d\theta}\right)_{\theta=\psi} P_\rho\ . \end{aligned} \tag{24}$$

The PSOS is defined now by the condition $\rho = 0$, corresponding to P_ρ in a predetermined branch (the negative one in present calculations) of the second-order equation for P_ρ that arises from the Hamiltonian conservation $H(\rho,\psi,P_\rho,P_\psi) = E$. Finally, all the PSS points are folded into the interval $\psi \in (0,180^\circ)$ to take into account the symmetry of the molecular system [29].

TABLE II. Numerical values of the coefficients in the Fourier series for the minimum energy path of Eq. (23).

λ	b_λ (a.u.)
0	4.132 893
1	0.234 366
2	0.485 224
3	–0.016 371 9
4	–0.058 797 0
5	0.006 220 71
6	0.015 145 6
7	–0.001 780 66
8	–0.004 312 50
9	0.000 255 183

C. The Jacobi metric

Given Hamiltonian Eq. (21), the inverse mass tensor is

$$(a^{ij}) = \begin{pmatrix} a^{RR} & a^{R\theta} \\ a^{\theta R} & a^{\theta\theta} \end{pmatrix}, \tag{25}$$

where $a^{RR} = \mu_1^{-1}$, $a^{\theta\theta} = (\mu_1 R^2)^{-1} + (\mu_2 r_e^2)^{-1}$, and $a^{R\theta} = a^{\theta R} = 0$. The Riemannian manifold, (M, g_{ij}), is defined as $M = \{(R,\theta) \in \mathbb{R}^2 / V(R,\theta) < E\}$ and $g_{ij}(R,\theta) = 2W\, a_{ij}(R,\theta)$, and the Christoffel symbols for the metric are

$$\begin{aligned} \Gamma^R_{RR} &= -\frac{1}{2W}\frac{\partial V}{\partial R} \\ \Gamma^R_{R\theta} &= \Gamma^R_{\theta R} = -\frac{1}{2W}\frac{\partial V}{\partial \theta} \\ \Gamma^R_{\theta\theta} &= \frac{\mu_2 R r_e^2\left[-2\mu_2 r_e^2 W + R\left(\mu_1 R^2 + \mu_2 r_e^2\right)\frac{\partial V}{\partial R}\right]}{2\left(\mu_1 R^2 + \mu_2 r_e^2\right)^2 W} \\ \Gamma^\theta_{RR} &= \frac{\left(\mu_1 R^2 + \mu_2 r_e^2\right)\frac{\partial V}{\partial \theta}}{2\mu_2 R^2 r_e^2 W} \\ \Gamma^\theta_{R\theta} &= \Gamma^\theta_{\theta R} = \frac{2\mu_2 r_e^2 W - R\left(\mu_1 R^2 + \mu_2 r_e^2\right)\frac{\partial V}{\partial R}}{2R(\mu_1 R^2 + \mu_2 r_e^2)W} \\ \Gamma^\theta_{\theta\theta} &= -\frac{1}{2W}\frac{\partial V}{\partial \theta}. \end{aligned} \tag{26}$$

Trajectories parametrized by physical time t are calculated integrating the equations

$$\begin{aligned} &\frac{d^2R}{dt^2} + \frac{1}{W}\left(\frac{\partial V}{\partial R}\frac{dR}{dt} + \frac{\partial V}{\partial \theta}\frac{d\theta}{dt}\right)\frac{dR}{dt} + \Gamma^R_{RR}\left(\frac{dR}{dt}\right)^2 \\ &\quad + 2\Gamma^R_{R\theta}\frac{dR}{dt}\frac{d\theta}{dt} + \Gamma^R_{\theta\theta}\left(\frac{d\theta}{dt}\right)^2 = 0, \\ &\frac{d^2\theta}{dt^2} + \frac{1}{W}\left(\frac{\partial V}{\partial R}\frac{dR}{dt} + \frac{\partial V}{\partial \theta}\frac{d\theta}{dt}\right)\frac{d\theta}{dt} + \Gamma^\theta_{RR}\left(\frac{dR}{dt}\right)^2 \\ &\quad + 2\Gamma^\theta_{R\theta}\frac{dR}{dt}\frac{d\theta}{dt} + \Gamma^\theta_{\theta\theta}\left(\frac{d\theta}{dt}\right)^2 = 0. \end{aligned} \tag{27}$$

D. The JLC equations

Concerning the geodesic deviation vector field, $\mathbf{J}(s) = J^1(s)\mathbf{e}_{(1)}(s) + J^2(s)\mathbf{e}_{(2)}(s)$, along the fiducial trajectory $\gamma(s)$, we obtain for the scalar J [remember here the change of variable made after Eq. (19)] the following JLC equation in terms of the physical time:

$$\frac{d^2J}{dt^2} - \frac{1}{W}\frac{dW}{dt}\frac{dJ}{dt} + 2W^2\hat{R}J = 0, \tag{28}$$

where the scalar curvature, $\hat{R}$, at any point in the manifold determines the local stability of the geodesics around the

fiducial, and it is given by

$$\hat{R} = \frac{1}{2W}\tilde{\mathcal{R}} + \frac{(N-1)}{8W^3}\{4W\nabla^2 V + (6-N)|\nabla V|^2\}, \quad (29)$$

N being the dimensionality of the system ($N = 2$ in our case), $\tilde{\mathcal{R}} = 6r_e^2\mu_2/(r_e^2\mu_2 + \mu_1 R^2)^2$ the scalar curvature for the space with metric $a_{ij}(R,\theta)$, $|\nabla V|^2 = a^{ij}\partial_i V \partial_j V$, and ∇^2 the Laplacian-Beltrami operator,

$$\nabla^2 V = a^{ij}\nabla_i\nabla_j V = a^{ij}\left(\frac{\partial^2 V}{\partial x^i \partial x^j} - \tilde{\Gamma}^k_{ji}\frac{\partial V}{\partial x^k}\right). \quad (30)$$

Here, $\tilde{\Gamma}^k_{ji}$ is the Christoffel symbol associated with the metric $a_{ij}(R,\theta)$,

$$\tilde{\Gamma}^R_{\theta\theta} = \frac{-r_e^4\mu_2^2 R}{\left(r_e^2\mu_2 + \mu_1 R^2\right)^2}, \quad \tilde{\Gamma}^\theta_{R\theta} = \tilde{\Gamma}^\theta_{\theta R} = \frac{r_e^2\mu_2}{\left(r_e^2\mu_2 + \mu_1 R^2\right)R}, \quad (31)$$

which render a Laplacian equal to

$$\nabla^2 V = a^{RR}\frac{\partial^2 V}{\partial R^2} + a^{\theta\theta}\frac{\partial^2 V}{\partial \theta^2} + \frac{r_e^2\mu_2}{\left(r_e^2\mu_2 + \mu_1 R^2\right)\mu_1 R}\frac{\partial V}{\partial R}. \quad (32)$$

Substituting all these expressions into Eq. (29), we obtain

$$\hat{R} = \frac{1}{2W}\frac{6r_e^2\mu_2}{\left(r_e^2\mu_2 + \mu_1 R^2\right)^2} + \frac{1}{2W^2}\left\{a^{RR}\frac{\partial^2 V}{\partial R^2} + a^{\theta\theta}\frac{\partial^2 V}{\partial \theta^2} + \frac{r_e^2\mu_2}{\left(r_e^2\mu_2 + \mu_1 R^2\right)\mu_1 R}\frac{\partial V}{\partial R}\right\} + \frac{1}{2W^3}\left\{a^{RR}\left(\frac{\partial V}{\partial R}\right)^2 + a^{\theta\theta}\left(\frac{\partial V}{\partial \theta}\right)^2\right\}. \quad (33)$$

The differential equations that need to be simultaneously integrated in our geometrical study are Eqs. (27) and (28). This is done numerically using a fourth-order Runge-Kutta method written in Fortran [30].

IV. RESULTS AND DISCUSSION

A. LiNC and LiCN classical trajectories

In this work we consider the vibrational dynamics of LiNC and LiCN at three different values of the excitation energy. These dynamics are monitored using the PSOS described in Sec. III B. The results are shown in the bottom panels of Fig. 2. As can be seen, at the lowest energy considered, $E = 1510.5$ cm^{-1} (see leftmost panel), the dynamics around

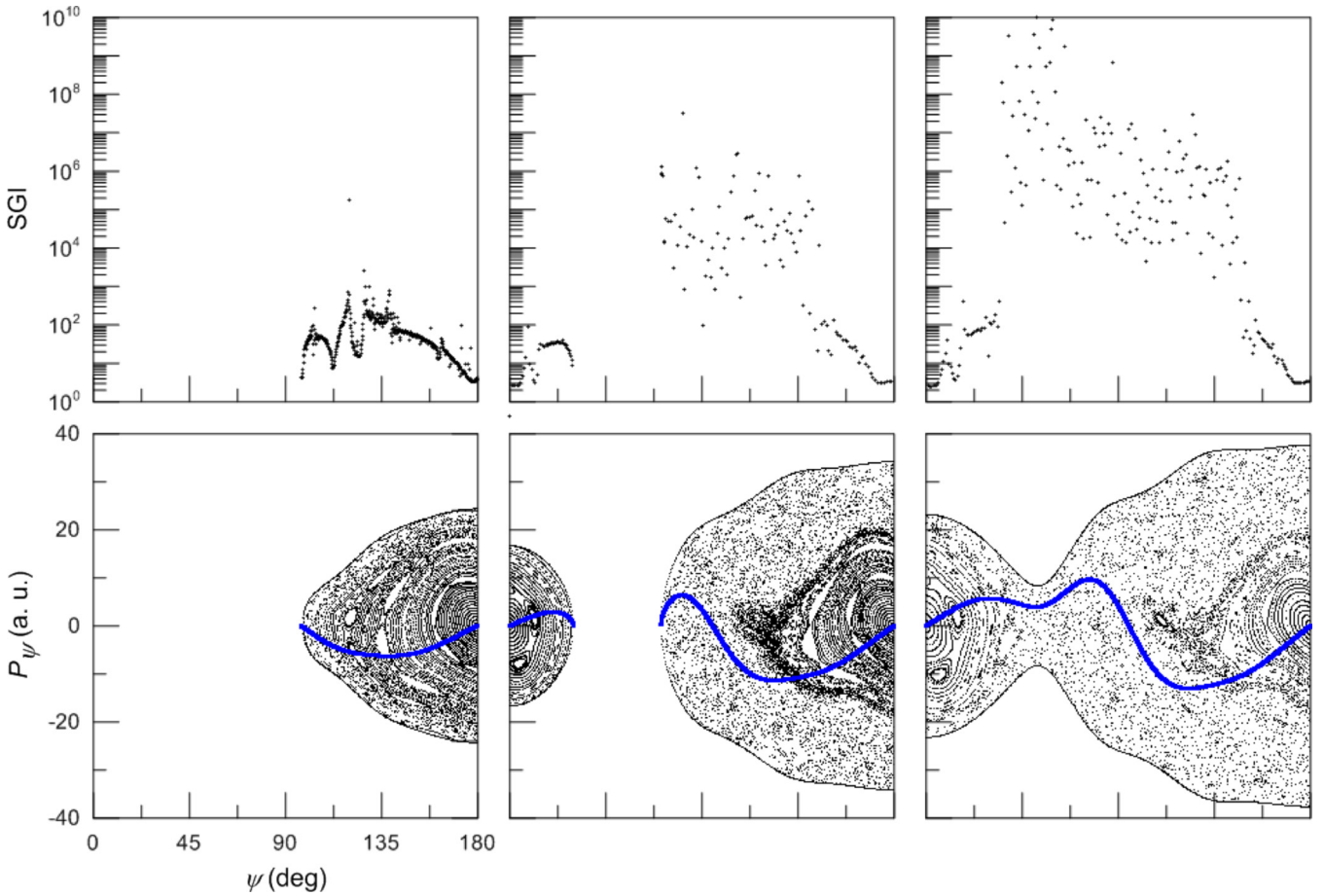

FIG. 2. (Color online) (Bottom) Composite Poincaré surfaces of section for the vibrational dynamics (see Sec. III B for details) for three different values of the energy: (left) $E = 1510.5$, (center) 2964.7, and (right) 3595.06 cm^{-1}, respectively. (Top) Numerical values of the SGI indicator at the same energies for different trajectories started at the surfaces of section below along the $\dot{\theta} = 0$ (blue) line (see discussion in Sec. IV C).

the LiNC ($\theta = 180^\circ$) is confined to invariant tori or chains of islands with narrow stochastic (chaotic) bands, since it is very regular. As the energy increases to 2964.7 cm^{-1} (see central panel) motion in the other well (LiCN at $\theta = 0$) is possible; it is very regular. Concerning the LiNC isomer at this higher energy, a big portion of the available phase space has become chaotic (in the most outer region), and a conspicuous accumulation of points is observed surrounding the regular region (inner part of the chaotic region); this being an indication of the existence of a cantorus or partial barrier for the flux of trajectories across [26]. Finally, at the largest energy considered (rightmost panel), the two wells are connected by rotating (isomerizing) trajectories. The previously mentioned cantorus appears to be more broken up, and chaos is more widespread, in general.

B. Geometrical method applied to LiNC and LiCN trajectories

In this subsection, we study some representative trajectories of the LiNC and LiCN isomerizing system, which will be analyzed using the geometrical method described in Secs. II B and III D. In particular, the evolution of the deviation vector will be considered.

We start with four representative trajectories propagated at $E = 1510.5$ cm^{-1}. The orbits, labeled red (a), blue (b), green (c), and pink (d), are shown in the upper four panels of Fig. 3, and the corresponding PSOS are presented at the bottom panel. As can be seen, they are all regular. The first three are located in the chain of islands associated to the resonance $\nu_R : \nu_\theta = 1{:}10$, being progressively [from red (a) to blue (b) to green (c)] farther apart from the center of the resonance. The last trajectory (d) is quasiperiodic, and it is confined in the torus plotted in pink visible in the lower panel. The evolution of J, the second component of vector $\mathbf{J}$ giving the deviation vector field of the four previous trajectories, are shown in the top four panels of Fig. 4. As can be seen, this quantity oscillates wildly with s, making the amplitude appear (approximately) modulated by two main frequencies of very different magnitude. To follow the overall behavior, we just take from these plots the points corresponding to the maxima in the low-frequency oscillations. To help in the discussion, we have marked these points with the same colors used in Fig. 3 for the trajectories, and we have joined them with straight connecting lines. The corresponding polylines, showing the overall behavior of J with s, are presented together for comparison in the bottom panel of the figure. As can be seen, the deviation from the fiducial trajectory is approximately constant for trajectory (a), which is very close to periodic motion, while it grows linearly with s for the remaining trajectories, resonant and quasiperiodic. Moreover, the largest slope corresponds to trajectory (c), which is the one farthest from the center of the resonance. This result is reasonable, since such a trajectory is the closest one to the band of stochasticity associated with this resonance, while the rest are all embedded into more regular motion. The extreme case is that of trajectory (a), which is almost at the center of the resonant island. Notice also that the slope for the quasiperiodic trajectory (d) is noticeably smaller than that for (c), a further confirmation of the performance of J as an indicator of regularity and chaos.

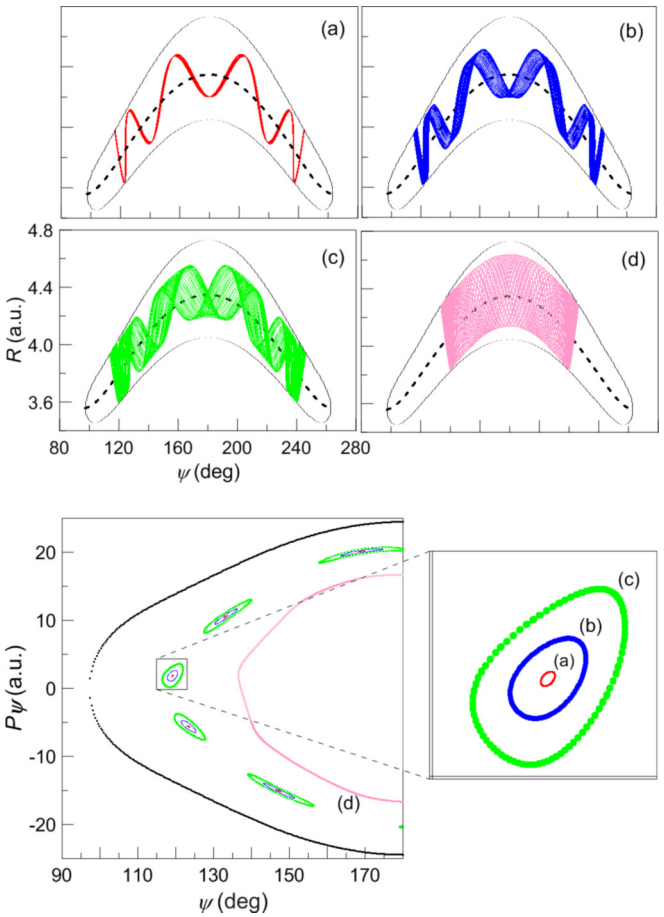

FIG. 3. (Color online) Four representative trajectories of LiNC and LiCN, labeled red (a), blue (b), green (c), and pink (d), and their corresponding Poincaré surface of section (bottom panel) for an energy $E = 1510.5$ cm^{-1}.

We consider next in Fig. 5 four representative trajectories at $E = 2964.7$ cm^{-1}. Three of them are regular, and they are located again in the chain of islands corresponding to the same 1:10 resonance discussed before; the fourth trajectory is a chaotic one. The corresponding PSOSs are shown in the upper left panel of the figure. Moreover, the orbit and deviation vector field J for the chaotic trajectory [pink or (d)] are also shown in the upper right and lower left panels of the figure, respectively. As can be seen, J grows exponentially in this case, thus allowing J to get a very large value at $s \gtrsim 800\,000$ a.u. (the value at which we stop all our trajectories), in contrast with what happens in the regular case, where the growth is only linear. Finally, the last panel of the figure shows, in a semilog scale, the overall behavior of J for the four trajectories we are considering. The same comments made above for $E = 1510.5$ cm^{-1} apply here for the regular trajectories. In contrast, the growth for the chaotic trajectory is here, as expected, much bigger and exponential (as opposed to the linear growth observed for the regular regime) than in all other cases.

Moreover, a close examination of the behavior of J for the chaotic trajectory reveals a very interesting behavior, showing the existence of three different regions having different values of the slope. Namely, up to $s \simeq 2.5 \times 10^5$ a.u. the trajectory starts with a definite value of the slope, after that the value of

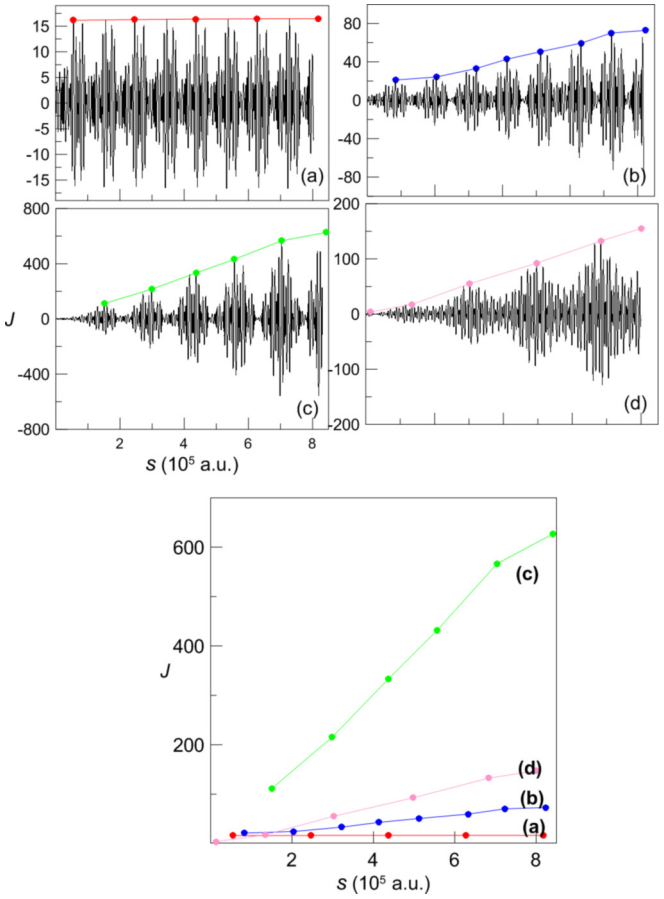

FIG. 4. (Color online) Evolution of the deviation vector field J with s for the four LiNC and LiCN trajectories (a)–(d) shown in Fig. 3 (same color code is maintained). The overall behavior, ascertained by taking the maxima in the oscillations of J, is presented in the bottom panel.

the slope diminishes, and later for $s \simeq 5.5 \times 10^5$ a.u. the slope increases recovering again the original value. This conspicuous change clearly indicates the existence of a peculiarity in the dynamics of this chaotic trajectory, which seems to evolve from a more chaotic regime to a less chaotic one, alternatively. To prove this conjecture, we have followed the (phase space) evolution of the trajectory in the three periods with the same value of the slope described above. The results are shown in Fig. 6, where it is clearly seen that in the different periods the trajectory is actually confined into very different regions of phase space. Namely, in the first and third periods, corresponding to $0 \lesssim s \lesssim 2.5 \times 10^5$ a.u. and $5.5 \times 10^5 \lesssim s \lesssim 8 \times 10^5$ a.u., respectively, the trajectory is confined in the outer part of the chaotic phase space region (see upper left panel of Fig. 5). However, in the intermediate period between them, i.e., $2.5 \times 10^5 \lesssim s \lesssim 5.5 \times 10^5$ a.u., the trajectory is confined into a narrow, inner part of that region, which is moreover closer to the regular part of phase space, this justifying why here the value of the slope of J is significantly smaller.

Obviously, the boundary between these two regions is the cantorus described by us in Refs. [26] and [27], which acts as a partial dynamical barrier in phase space [31,32]. These phase space structures are very important in the vibrations of small molecules since they may play a key role in the control of the

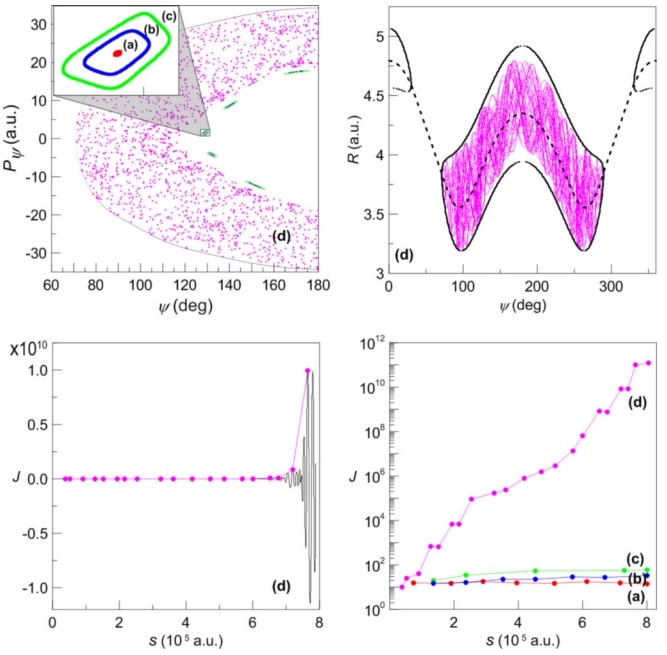

FIG. 5. (Color online) Same as described in the legends of Figs. 3 and 4 for $E = 2964.7$ cm^{-1}. The Poincaré surfaces of section are given in the upper left panel, the orbit of the chaotic [pink or (d)] trajectory and the corresponding J vs. s plot are presented in the upper right and lower left panels, respectively, and the overall behavior of J for the four trajectories can be seen in the lower right panel (notice the semilog scale here).

intramolecular energy relaxation that usually leads to chemical reactivity. Actually, they are responsible for many nonstatistical effects that should be taken into account in statistical theories, such as that of Rice-Ramsperger-Kassel-Marcus [33]. The presence of cantori implies the existence of long time correlations and slow relaxation of the dynamics in chaotic regions of phase space. This causes some trajectories to become temporarily trapped inside or outside these barriers for many vibrational periods. This time is usually long compared to that dictated by the Lyapunov exponential separation of trajectories.

C. The SGI for the LiNC and LiCN molecular system

In this subsection we discuss the performance of the SGI introduced in Sec. II B. We calculate and compare this indicator

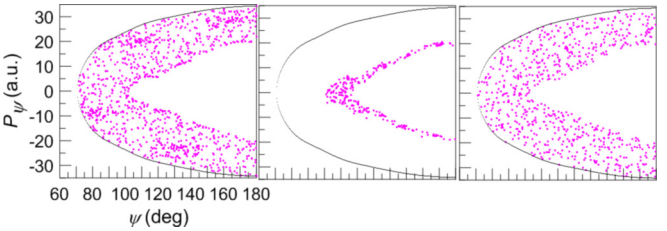

FIG. 6. (Color online) Influence of the cantori existing at $E = 2964.7$ cm^{-1} [26,27], which acts as a partial barrier for the flux of trajectories in phase space, implying that a typical trajectory visits alternatively the corresponding outer and inner regions with different dynamical characteristics. This effect is responsible for the slope changes found in the corresponding J vs. s plot shown in Fig. 5.

for trajectories with different values of the vibrational energy and initial conditions, in a systematic way. For this purpose, we examine a set of trajectories extracted from those used to construct the PSOS in the bottom panels of Fig. 2. In particular, we take the orbits starting with $\rho = 0$, i.e., on the minimum energy path of the LiNC and LiCN potential energy surface (dashed line in Fig. 1) and null angular velocity, $\dot{\theta} = 0$. This choice is equivalent to taking

$$P_\psi(\dot{\theta} = 0) = -\sqrt{2\{E - V[R_e(\theta),\theta]\}\, a_{RR}}\, \frac{dR_e(\theta)}{d\theta}, \quad (34)$$

and the corresponding values are shown as a function of ψ (blue lines) in the bottom panels of Fig. 2. The values of the SGI are computed after each trajectory has completed a total length of $s = 8 \times 10^8$ a.u. In this way, a global map for the stability of the system is obtained, which can also be compared in our case with the results of the corresponding composite PSOSs. The results are presented in the top panels of Fig. 2.

Let us start the discussion with the left panel of Fig. 2, which corresponds to the lowest energy considered, $E = 1510.5$ cm^{-1}, where the dynamics is almost all regular, as ascertained from the PSOS observation. This fact is reflected in the low values observed for the SGI. Moreover, the SGI is continuous, showing also a (relatively) smooth variation with the variable ψ. The exception occurs in the neighborhoods of the resonance, where the value at the center is smaller (local minimum) and it gets sharply larger at the sides (as discussed in the previous subsection), thus forming a kind of (very irregular) "M" shape figure. This behavior is more conspicuous in the middle and left part of the curve, and it can probably be made into a method to locate the corresponding periodic orbits. When considering the middle panel, corresponding to an energy of $E = 2964.7$ cm^{-1}, we have the same behavior in the regular regions, i.e., in the right end of the curve corresponding to the LiNC isomer and also the new part at the extreme left corresponding to the LiCN isomer. In the latter, the M-shape corresponding to the 1:4 resonance is clearly visible. However, at this energy we have a large region of irregular or chaotic behavior, where the SGI is much bigger and appears completely noncontinuous due to wild oscillations. Finally, in the rightmost panel we consider the biggest energy, $E = 3595.6$ cm^{-1}, which corresponds to the largest observed chaotic region, now including the region associated to the saddle in the potential energy surface separating the two isomers. The two potential wells are connected at this energy, which implies the appearance of isomerizing trajectories. As a result, the dynamics are more chaotic, particularly in this latter region, and accordingly the SGI values are larger. Actually, two distinct parts in the chaotic region, with different values of this index, are clearly distinguished. In the left part located over the saddle of the potential energy surface, where the dynamics are more irregular due to the presence of the corresponding unstable fixed point, the SGI is bigger than in the part at the right, which is closer to the LiNC isomer, which has a regular dynamics.

V. CONCLUSIONS

In this work, we have studied the vibrational dynamics of the LiNC and LiCN isomerizing system described by a realistic 2D model from a geometrodynamical perspective, studying the stability of representative trajectories of this system at different values of the excitation energy.

For this purpose, we have defined a stability geometrical indicator, SGI, which is able to clearly distinguish regular from chaotic behavior. Indeed, in the former case, the SGI is continuous and bounded, while in the latter the values for the SGI are noncontinuous and unbounded. This SGI can also be used to efficiently compute periodic orbits, since it presents local minima around the associated chain of islands.

Finally, let us remark that the approach presented here can be extended in a natural way to study this, and other similar realistic systems, in more than two dimensions. As discussed above, this type of study is interesting and important to ascertain intramolecular vibrational relaxation mechanisms and processes, as well as chemical reactivity. However, this extension is not straightforward, since in this case the evolution of **J** depends on the dynamics, and then on the knowledge (history) of the plane (which rotates along the trajectory) in which the curvature is computed.

ACKNOWLEDGMENT

This research was supported by the Ministry of Economy and Competitiveness-Spain under Contract No. MTM2012-39101.

[1] See, for example, F. Borondo and R. M. Benito, in *Frontiers of Chemical Physics*, edited by E. Yurtsever, NATO ASI Series C (Kluwer, Dordrecht, 1995), and references therein.
[2] R. Schinke, *Photodissociation Dynamics* (Cambridge University Press, Cambridge, 1992).
[3] H. L. Dai and R. W. Field (editors), *Molecular Dynamics and Spectroscopy by SEP* (World Scientific, Singapore, 1995).
[4] Edited by A. Zewail, *The Chemical Bond: Structure and Dynamics* (Academic Press, San Diego, 1992).
[5] See, for example, Ch. Skokos, Lect. Notes Phys. **790**, 63 (2010).
[6] E. Lega, M. Guzzo, and C. Froeschlé, Physica D **182**, 179 (2003).
[7] R. Barrio, Chaos Solitons Fractals **25**, 711 (2005).
[8] H. S. Dumas and J. Laskar, Phys. Rev. Lett. **70**, 2975 (1993).
[9] Ch. Skokos, Ch. Antonopoulos, T. C. Bountis, and M. N. Vrahatis, J. Phys. A **37**, 6269 (2004).
[10] F. J. Arranz, F. Borondo, and R. M. Benito, Chem. Phys. Lett. **317**, 451 (2000).
[11] R. Sospedra-Alfonso, L. Velazquez, and J. Rubayo-Soneira, Chem. Phys. Lett. **375**, 261 (2003).
[12] L. Casetti, M. Pettini, and E. G. D. Cohen, Phys. Rep. **337**, 237 (2000).
[13] M. Pettini, *Geometry and Topology in Hamiltonian Dynamics and Statistical Mechanics*, IAM Series 33 (Springer, New York, 2007).

[14] L. P. Eisenhart, Ann. Math. **30**, 591 (1929).
[15] P. Cipriani and M. Di Bari, Phys. Rev. Lett. **81**, 5532 (1998).
[16] L. Horwitz, Y. B. Zion, M. Lewkowicz, M. Schiffer, and J. Levitan, Phys. Rev. Lett. **98**, 234301 (2007).
[17] Y. BenZion and L. Horwitz, Phys. Rev. E **76**, 046220 (2007); **78**, 036209 (2008); **81**, 046217 (2010).
[18] M. Pettini, Phys. Rev. E **47**, 828 (1993).
[19] L. Casetti, R. Livi, and M. Pettini, Phys. Rev. Lett. **74**, 375 (1995).
[20] L. Casetti and M. Pettini, Phys. Rev. E **48**, 4320 (1993).
[21] M. Cerruti-Sola and M. Pettini, Phys. Rev. E **53**, 179 (1996).
[22] L. Casetti, C. Clementi, and M. Pettini, Phys. Rev. E **54**, 5969 (1996).
[23] M. Cerruti-Sola and M. Pettini, Phys. Rev. E **51**, 53 (1995).
[24] M. P. do Carmo, *Riemannian Geometry* (Birkhäuser, Boston, 1992).
[25] M. Di Bari, D. Boccaletti, P. Cipriani, and G. Pucacco, Phys. Rev. E **55**, 6448 (1997).
[26] F. Borondo, A. A. Zembekov, and R. M. Benito, Chem. Phys. Lett. **246**, 421 (1995); J. Chem. Phys. **105**, 5068 (1996); **107**, 7934 (1997).
[27] J. C. Losada, J. M. Estebaranz, R. M. Benito, and F. Borondo, J. Chem. Phys. **108**, 63 (1998); F. Borondo, J. C. Losada, and R. M. Benito, Found. Phys. **31**, 147 (2001); J. C. Losada, R. M. Benito, F. J. Arranz, and F. Borondo, Int. J. Quantum Chem. **86**, 167 (2002).
[28] R. Esser, J. Tennyson, and P. E. S. Wormer, Chem. Phys. Lett. **89**, 223 (1982).
[29] R. M. Benito, F. Borondo, J.-H. Kim, B. G. Sumpter, and G. S. Ezra, Chem. Phys. Lett. **161**, 60 (1989).
[30] W. H. Press, S. A. Teukolsky, W. T. Vetterling, and B. P. Flannery *Numerical Recipes: The Art of Scientific Computing* (Cambridge University Press, Cambridge, MA, 2007).
[31] R. S. MacKay, J. D. Meiss, and I. C. Percival, Physica D **13**, 55 (1984).
[32] D. Bensimon and L. P. Kadanoff, Physica D **13**, 82 (1984).
[33] M. J. Davis, J. Phys. Chem. **92**, 3124 (1988).